Evidence of Branching Phenomena in Current-Driven Ionization Waves

Keith T. K. Loebner,* Thomas C. Underwood, and Mark A. Cappelli
High Temperature Gasdynamics Laboratory, Stanford University, Stanford, California 94305, USA
(Received 10 April 2015; published 19 October 2015)

This Letter reports the first fully consistent experimental observations of current-driven ionization waves conforming to the magnetohydrodynamic Rankine-Hugoniot model for hydromagnetic shocks. Detailed measurements of the thermodynamic and electrodynamic plasma state variables across the ionization region confirm the existence of two types of waves, corresponding to the upper and lower solution branches of the Hugoniot curve. These waves are generated by pulsed currents in a coaxial gas-fed plasma accelerator. The coupling between the state variables of this complex, transient, three-dimensional system shows a remarkable quantitative agreement of less than 8% deviation from the quasisteady, one-dimensional theoretical model.

DOI: 10.1103/PhysRevLett.115.175001 PACS numbers: 52.25.Xz, 52.30.Cv, 52.50.Lp, 52.59.Dk

Current-driven magnetohydrodynamic (MHD) ionization waves and acceleration mechanisms are a key feature of many natural and artificial plasma systems. These processes provide pathways for the coupling of magnetic, thermal, and kinetic energy modes in magnetized plasmas, strongly impacting their behavior. The magnetic pressure gradients produced as a consequence of such waves have been shown to have an essential role in the generation of astrophysical jets [1–4]. These waves also underpin the formation and acceleration of spheromak and compact toroid plasmas [5–10], as well as the recent advances in plasma-jet driven magnetized target fusion and shear-flow-stabilized Z pinch schemes [11–13]. Because of increasing interest in these plasma phenomena, there is a critical need for a reliable model that accurately predicts the behavior of plasmas formed and sustained by MHD ionization waves.

In this Letter, we present observations of current-driven ionization waves that appear to mimic the behavior of classical combustion-driven shocks described by the Rankine-Hugoniot relations. We collect concurrent, time-resolved experimental data capturing the MHD field variables both upstream and downstream of current-driven ionization waves, in order to determine the wave jump conditions. We use this information to compare our data against conditions predicted by a modified set of the Rankine-Hugoniot relations for MHD shock waves [14,15], and not only observe the two distinct wave types predicted by the theory, but also obtain excellent quantitative agreement among the measurable flow parameters for both types of waves.

The plasma source employed for this Letter is the Stanford Plasma Gun Experiment [16], shown schematically in Fig. 1(a). This device is a 26 cm long, 5 cm diameter, coaxial pulsed Lorentz force plasma accelerator, a configuration that has been used extensively in earlier work [15,17–21]. During operation, breakdown is initiated by the injection of a nitrogen gas puff into the breach end of the accelerator [the left side in Fig. 1(a)], the electrodes of which are held at high voltage in vacuum. Thus, the interelectrode region approaches the Paschen curve from the vacuum side, and initial breakdown occurs as the pressure rises above the critical value. The current is driven by a 56 μF capacitor bank, initially charged to 3 kV, such that the current and voltage waveforms are decaying sinusoids [an example current trace is shown in Fig. 1(b)] that lead to a second breakdown event corresponding to the second half-period of oscillation.

The downstream plasma state is measured using a quadruple Langmuir probe (QLP) in current-saturation mode [22], which provides the plasma density and temperature at high spatial and temporal resolution. The probe consists of four independent electrodes, biased relative to one another as shown in Fig. 1(a), and supported by an insulating ceramic substrate. Electrodes 1, 2, and 4 are oriented parallel to the flow direction, while electrode 3 is perpendicular to the flow direction. The plasma currents collected by electrodes 2, 3, and 4 are measured via wideband Pearson current monitors, and the current collected by electrode 1 is calculated via a current balance between the four electrodes. Conversion of the measured currents and bias voltages to the plasma state variables is accomplished by the solution of a nonlinear system of equations derived from kinetic theory [23], and developed for this particular probe configuration to provide plasma temperature T_e, plasma density n_e, plasma potential ϕ, and ion thermal Mach number S_i [22,24]. Example collected probe currents are shown in Fig. 1(b), and example solution vectors for plasma density and plasma temperature are shown in Figs. 1(c) and 1(d).

The experimental procedure for collecting the QLP data was as follows: with the probe at a given axial position of the linear stage [shown in Fig. 1(a)], the accelerator was fired and the probe currents were measured for the duration of the drive current ringdown time (including both the

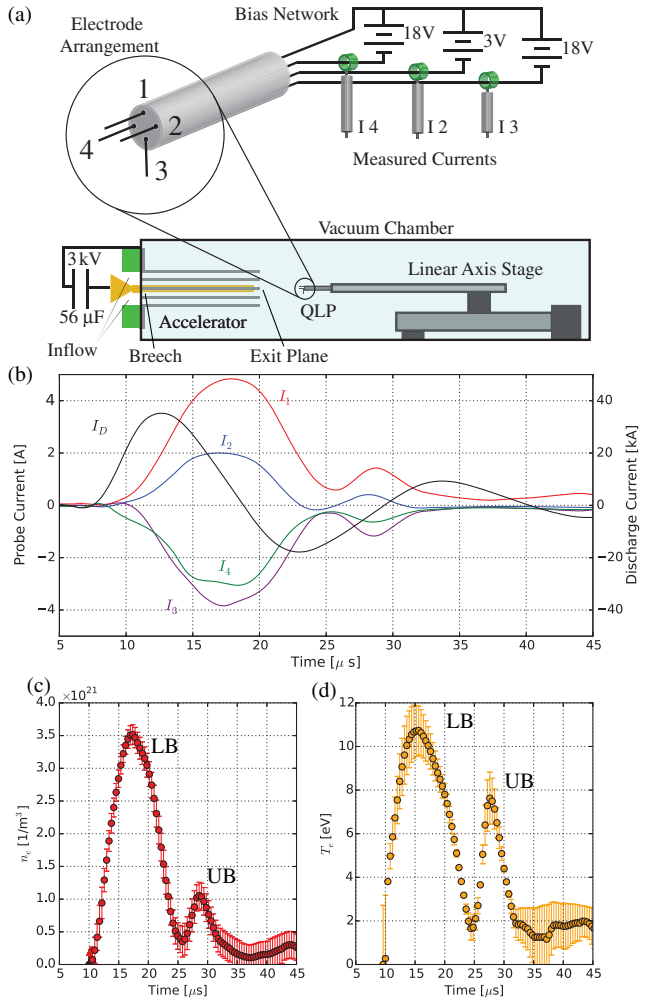

FIG. 1 (color online). (a) Schematic of the experimental setup. (b) An example time series of all three measured probe currents, the fourth probe current calculated via current balance, and the discharge current (alternate y axis). (c) Calculated plasma density time series for an example probe location. (d) Calculated plasma temperature time series for the example probe location.

primary and secondary breakdown events). The QLP was then traversed along the accelerator axis in increments of 5 mm, and the process was then repeated in order to sample axial locations between 50 and 215 mm from the accelerator exit plane. A repeatability study was also conducted, and the magnitude of the measured currents was found to vary by less than 1% from shot to shot at a single axial position (for details of the spatial and temporal resolution of the probe, see Supplemental Material [24]). Thus, this axial-scan technique enabled the acquisition of representative spatiotemporal contours of the plasma parameters along the accelerator axis, downstream of the exit plane, for the consecutive ionization waves.

The velocity of the accelerated plasma is determined from the slope of the leading edge of the spatiotemporal plasma density contours, providing another key state variable. Other important information necessary to fully describe the plasma state, but not collected directly by the QLP, include: the upstream conditions for the first ionization wave (i.e., the injected gas conditions) and the magnetic pressure profile as a function of time and space. The former was measured at the injection location using piezoelectric pressure transducers [25], and the upstream plasma density was thus obtained assuming full ionization. The latter was calculated by averaging the theoretical azimuthal field (based on the measured discharge current) over the radius of the plasma accelerator to obtain a spatially averaged field strength as a function of time [24].

A typical pair of discharge events is shown in Fig. 2 as a series of intensified CCD images. A first ionization wave forms at the breech end of the accelerator and rapidly broadens to fill the coaxial electrode volume (region I), continuing to accelerate plasma in the axial direction downstream once it has fully developed (region II). As the current decays and crosses zero, the first wave dissipates and a second ionization wave forms at the breach (region III). This second wave (i.e., a current sheet) propagates into the gas left behind by the preceding ionization wave and is expelled from the accelerator (region IV).

Two distinct wave modes are clearly visible in Fig. 2, which we hypothesize to correspond to the upper and lower branch solutions of the Rankine-Hugoniot jump conditions. The upper branch (UB) solutions (or "detonations" in the case of chemically reacting gas flows) are known to occur

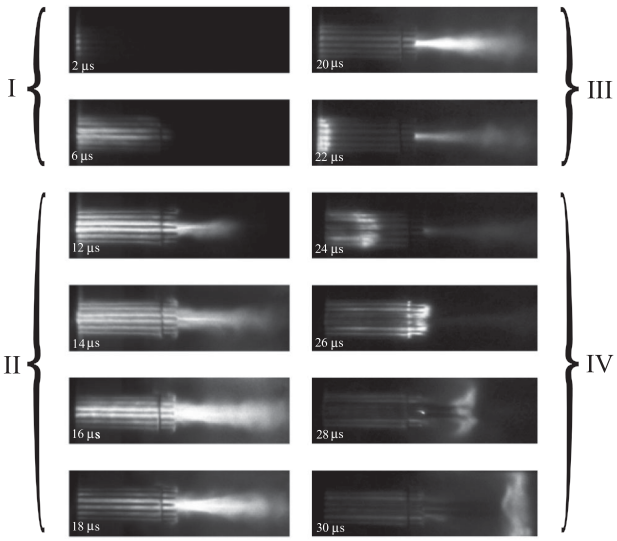

FIG. 2. ICCD images of consecutive current-driven ionization waves. I. Establishment of the lower branch ionization wave in the coaxial accelerator volume, broadening towards exit plane. II. Acceleration and expulsion of the plasma through the stationary lower branch ionization wave. III. Formation of the upper branch wave at the breach of the accelerator as the lower branch wave dissipates. IV. Propagation of the upper branch ionization wave along the accelerator axis. The dark silhouetted lines are the anode rods, as shown in Fig. 1(a). Time stamps are correlated with the contour in Fig. 3.

when the pressure and density increase across the wave. These waves consist of a shock front followed by an expansion wave, and typically manifest as relatively sharp discontinuities in the flow. Different characteristics are observed in the lower branch (LB) solutions, also known as "deflagrations," wherein the pressure and density decrease across the wave. In contrast, LB waves are broader, propagate slowly, and produce higher accelerated gas velocities due to the lack of a decelerating normal shock. As shown in Fig. 2, the consecutive waves appear to be a LB wave followed by an UB wave: the first wave (regions I and II) is broad and approximately stationary in the laboratory frame while accelerating the plasma in a jet downstream. The second wave (regions III and IV) is a narrow current sheet, and propagates away from the breach into the upstream residual gas left by the LB wave before being expelled.

The two distinct events are also evident in the z-t plasma density contours derived from the QLP data, shown in Fig. 3. The dotted white lines indicate the leading edges of the contours corresponding to the first and second ionization waves, which were used to determine the accelerated plasma velocities in each case. The plasma plume resulting from the first wave is broad in time, and expands as it moves axially downstream. The second wave is narrower in time, and the plume moves downstream at a slower velocity. These characteristics are consistent with the two solution branches of the Rankine-Hugoniot relations, and strongly suggest they govern the dynamics of the system.

For a quantitative comparison, we require expressions relating the jump conditions across each type of wave in terms of the measured quantities (i.e., density, total pressure, and velocity). We have chosen the fixed-frame accelerated plasma velocity as the "output" variable for comparison, so our expressions relate the downstream plasma velocity directly to the other state variables in both cases. An illustration of the LB and UB ionization wave processes is shown in Fig. 4, and a detailed derivation is contained in the Supplemental Material [24]. Flow velocities in the frame moving with the wave are represented by a u, velocities in the laboratory frame by a V, and "upstream" is the direction in which the wave propagates (along the acceleration direction in the UB case, and opposing the acceleration direction in the LB case).

The velocity of the plasma downstream of the LB wave is obtained by combining the mass and momentum conservation equations relating the wave-frame upstream and downstream plasma velocities (u_u and u_d, respectively). We observe the LB waves to move slowly in the laboratory frame, such that the wave velocity V_w can be considered constant. The upstream velocity V_u is typically much less than the downstream velocity $V_{d_{\mathrm{LB}}}$, which is thus approximately given by

$$V_{d_{\mathrm{LB}}} \approx u_d - u_u = \sqrt{\left(\frac{1}{\rho_u} - \frac{1}{\rho_d}\right)(p_d^* - p_u^*)}, \qquad (1)$$

where the u and d subscripts represent the upstream and downstream conditions, respectively, ρ is the mass density, and p^* includes the magnetic pressure term, i.e.,

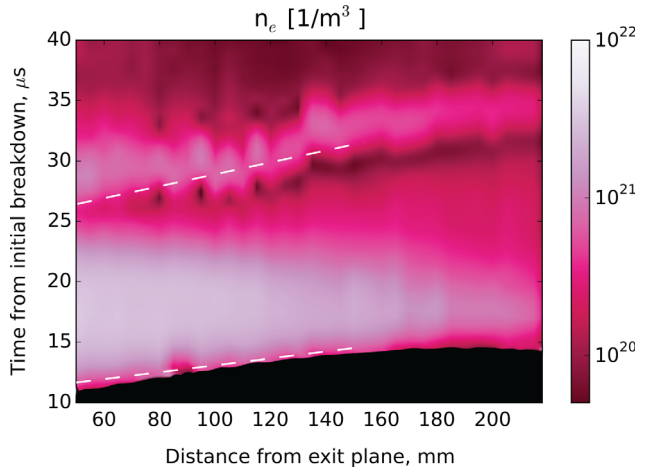

FIG. 3 (color online). Contours of free electron density in z-t space, shown as a function of distance from the accelerator exit plane in the axial direction and time from initial breakdown following primary gas injection. Regions of space and time in which the QLP equation system did not converge (i.e., no currents were being collected from the plasma) are represented by the black area in the lower portion of the figure. The leading edge contours of both waves are highlighted in Fig. 5.

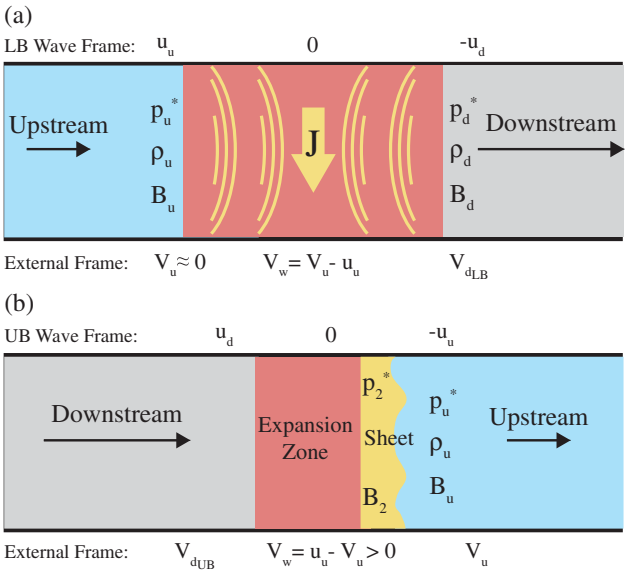

FIG. 4 (color online). Schematic representation of the lower and upper branch wave processes in one dimension. The breach end of the accelerator is to the left of each figure, and the exit plane is to the right. The larger flow vectors indicate the region in which the plasma has been accelerated. (a) A LB ionization wave, comprising a broad current conducting zone between the upstream and downstream regions. (b) An UB ionization wave, comprising a thin current sheet followed by an expansion region.

$$p^* = p_0 + \frac{B^2}{2\mu_0}, \tag{2}$$

in which B represents the local vacuum magnetic field strength and p_0 is the stagnation pressure. Note that Eq. (2) is valid in this form only when the direction of B is perpendicular to the flow. The validity of the $V_u \approx 0$ assumption is determined *ex post facto* based on calculation of the relevant parameters on the right-hand side of Eq. (1) from experimentally obtained values.

The expression for the downstream plasma velocity of the UB ionization wave is more complex, as the wave consists of the multiple distinct regions shown in Fig. 4(b): a current sheet that propagates into the upstream gas, followed by an expansion zone that accelerates the shock-heated, ionized gas. The strength of the hydromagnetic shock is a free parameter, which we call alpha (α), that dictates the matching condition between the shock and expansion regions. Thus, the upper and lower limits of the processed gas velocity are determined by the variation of α between $\alpha_{\min} < \alpha < 1$. The minimum value of α is determined by matching p_2^* and p_d^*, which corresponds to the weakest allowable expansion zone and gives

$$\alpha_{\min} = u_2 \sqrt{\frac{\rho_2}{\gamma p_2^*}}, \tag{3}$$

where γ is the specific heat ratio of the process gas. The expression for the processed gas velocity corresponding to the upper branch ionization wave, given a particular α, is given by

$$V_{d_{\mathrm{UB}}} = \frac{p_2^* - p_u^* + \frac{\alpha^2\gamma}{\alpha^2\gamma+1}\left(\frac{\rho_u}{\rho_2} p_u^* - p_2^*\right)}{\sqrt{(p_2^* - p_u^*)\rho_u\left(1 - \frac{\rho_u}{\rho_2}\right)}}. \tag{4}$$

Given Eqs. (1) and (4), we combine the experimentally determined state variables on the right-hand side of each equation in order to obtain the predicted downstream velocity for each type of wave. For the LB wave, the downstream pressure is calculated assuming the plasma equation of state to be $p_d^* = n_e k_B T_e$, consistent with observations by Woodall *et al.* that the downstream plasma has very little entrained radial current and magnetic flux [17]. For the UB wave, the time at which the current sheet is formed is determined using the discharge current trace, and the upstream conditions are derived from the QLP data corresponding to that time. The pressure in region II is again assumed to be dominated by the magnetic component, obtained via the measured discharge current. Given p_2^*, the hydromagnetic Mach number of the UB wave can be calculated, allowing ρ_2 to be determined from the adiabatic hydromagnetic shock jump equations. For all downstream measurements of plasma density, we renormalize the density to a Gaussian integral over the radial profile with the axial value as the peak, consistent with the observed radial falloff in bulk plasma emission ($\propto n_e^2$).

The comparison between the predicted and measured downstream velocities for both waves is shown in Fig. 5. For numerical values used in the calculation, see the Supplemental Material [24]. The total pressure and density both decrease across the first wave, indicating that this event is, indeed, a LB solution. The second wave exhibits the opposite behavior, acting as a magnetic piston that ionizes and compresses the upstream gas. The predicted accelerated plasma velocity for the LB case is within 8% of the measured value, while the measured velocity of the downstream plasma accelerated by the UB wave falls within the narrow range of predicted velocities, as indicated by the shaded region of Fig. 5(b). The measured velocity corresponds to a strength parameter of $\alpha \simeq 0.74$.

This remarkable quantitative agreement between the complex experimental system and the one-dimensional, steady-state MHD Rankine-Hugoniot model has significant implications for the continued study of these wave phenomena. The evident subordination of higher-dimensional and unsteady effects to the straightforward relationships captured by the model indicate that the dominant acceleration mechanism, particularly for the LB wave, is a highly efficient expansion of magnetic pressure into directed kinetic energy. It is also of note that an UB wave always forms subsequent to the LB wave, instead of vice versa. The Rankine-Hugoniot model predicts that this should occur; the first wave expands into vacuum downstream, and will thus experience a density and pressure drop across the wave, rendering it a LB solution. The second wave, by contrast, necessarily must propagate into the conditions left behind by the LB wave, which leads a compressive shock to form thus rendering it an UB solution.

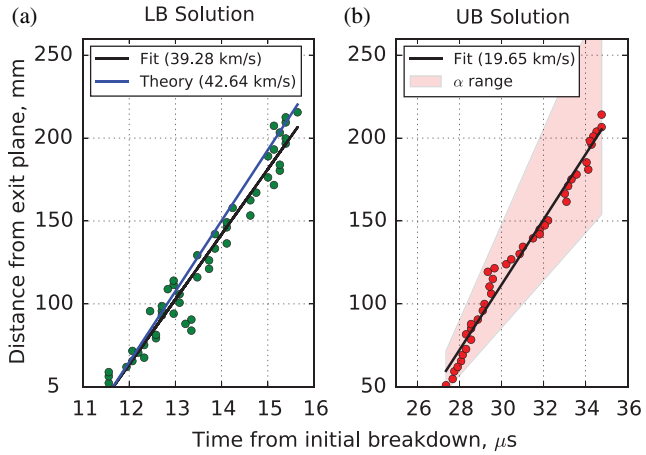

FIG. 5 (color online). Comparison of the measured density front velocity and theoretically calculated downstream velocity for the (a) lower branch solution and (b) upper branch solution. The range of theoretically allowable downstream velocities for the upper branch case are shown for $\alpha_{\min} < \alpha < 1$. Data values are specific contours of the leading edges of the two events shown in Fig. 3, displayed with corresponding linear fits.

This evidence of branching phenomena in consecutive current-driven ionization waves is strong support for consistency between these systems and the MHD Rankine-Hugoniot model. Such consistency is not typically expected for such complex systems, and while fully capturing the three dimensional, multiscale and nonequilibrium mechanisms underlying these processes may require involved numerical simulations, we have shown that good agreement can be obtained from a straightforward theoretical description. The MHD Rankine-Hugoniot model has thus been convincingly demonstrated to be a practical quantitative tool for the analysis of current-driven ionization waves.

This work is supported by the U.S. Department of Energy Grant No. DE-NA0002011. K. Loebner and T. Underwood gratefully acknowledge the financial support of the National Defense Science and Engineering Graduate Fellowship Program. The authors would also like to thank Dr. N. Gascon and Dr. A. Lucca Fabris for their insightful discussions, Dr. F. Poehlmann for his assistance with the ICCD imaging, and all other members of the Stanford Plasma Physics Laboratory who have provided help and guidance to our work.

*kloebner@stanford.edu

[1] J. Contopoulos, Astrophys. J. **450**, 616 (1995).
[2] D. L. Meier, S. Koide, and Y. Uchida, Science **291**, 84 (2001).
[3] P. M. Bellan, S. You, and S. C. Hsu, Astrophys. Space Sci. **298**, 203 (2005).
[4] J. S. T. Ng and R. J. Noble, Phys. Rev. Lett. **96**, 115006 (2006).
[5] P. B. Parks, Phys. Rev. Lett. **61**, 1364 (1988).
[6] J. H. Hammer, C. W. Hartman, J. L. Eddleman, and H. S. McLean, Phys. Rev. Lett. **61**, 2843 (1988).
[7] R. Raman, F. Martin, B. Quirion, M. St-Onge, J. L. Lachambre, D. Michaud, B. Sawatzky, J. Thomas, A. Hirose, D. Hwang, N. Richard, C. Côté, G. Abel, D. Pinsonneault, J. L. Gauvreau, B. Stansfield, R. Décoste, A. Côté, W. Zuzak, and C. Boucher, Phys. Rev. Lett. **73**, 3101 (1994).
[8] R. Raman *et al.*, Nucl. Fusion **37**, 967 (1997).
[9] H. S. McLean, D. Q. Hwang, R. D. Horton, R. W. Evans, S. D. Terry, J. C. Thomas, and R. Raman, Fusion Sci. Technol. **33**, 252 (1998).
[10] D. Kumar and P. M. Bellan, Phys. Rev. Lett. **103**, 105003 (2009).
[11] J. T. Cassibry, R. J. Cortez, S. C. Hsu, and F. D. Witherspoon, Phys. Plasmas **16**, 112707 (2009).
[12] J. Cassibry, Y. Thio, and S. Wu, Phys. Plasmas **13**, 053101 (2006).
[13] U. Shumlak and C. W. Hartman, Phys. Rev. Lett. **75**, 3285 (1995).
[14] G. W. Sutton and A. Sherman, *Engineering Magnetohydrodynamics* (McGraw-Hill, New York, 1965), p. 548.
[15] D. Y. Cheng, Nucl. Fusion **10**, 305 (1970).
[16] K. T. K. Loebner, B. C. Wang, F. R. Poehlmann, Y. Watanabe, and M. A. Cappelli, IEEE Trans. Plasma Sci. **42**, 2500 (2014).
[17] D. M. Woodall and L. K. Len, J. Appl. Phys. **57**, 961 (1985).
[18] S. Zhi-Gang, L. Cheng-Hui, L. Chun-Hian, W. Cheng, and Y. Size, J. Phys. D **28**, 2 (1995).
[19] H. Bruzzone and J. Martínez, Plasma Sources Sci. Technol. **10**, 471 (2001).
[20] V. I. Tereshin, A. N. Bandura, O. V. Byrka, V. V. Chebotarev, I. E. Garkusha, I. Landman, V. A. Makhlaj, I. M. Neklyudov, D. G. Solyakov, and A. V. Tsarenko, Plasma Phys. Controlled Fusion **49**, A231 (2007).
[21] F. R. Poehlmann, M. A. Cappelli, and G. B. Rieker, Phys. Plasmas **17**, 123508 (2010).
[22] N. Gatsonis and L. Byrne, IEEE Trans. Plasma Sci. **32**, 2118 (2004).
[23] S. Chen and T. Sekiguchi, J. Appl. Phys. **36**, 2363 (1965).
[24] See Supplemental Material at http://link.aps.org/supplemental/10.1103/PhysRevLett.115.175001 for detailed results of repeatability study and parameter values used in the calculation of wavefront velocities.
[25] K. T. K. Loebner, T. C. Underwood, and M. A. Cappelli, Rev. Sci. Instrum. **86**, 063503 (2015).